J. Iron Steel Res. Int. (2018) 25:1068–1077
https://doi.org/10.1007/s42243-018-0155-7

ORIGINAL PAPER

Microstructure evolution and mechanical properties of 316L austenitic stainless steel with aluminum addition by warm rolling

Xin Guo[1,2] · Pei-qing La[1,2] · Heng Li[1] · Yu-peng Wei[1] · Xue-feng Lu[2]

Received: 13 July 2017 / Revised: 18 September 2017 / Accepted: 10 October 2017 / Published online: 3 October 2018

Abstract
Microstructure evolution and mechanical properties of 316L austenitic stainless steel with aluminum addition by warm rolling at 550 °C were investigated. It is found that sample is composed of an ashen austenite matrix, a gray black ferrite phase and a small number of NiC_x. The average grain sizes are 21.62, 19.66 and 19.49 μm for samples with the rolling deformation of 30%, 50% and 70%, respectively. The yield strength and tensile strength of samples with solid solution time of 30 min and deformation of 70% are higher. The fracture modes are similar and belong to toughness fracture. The fracture surfaces of the samples are composed of relatively large equal-axis ductile dimples (5–15 μm) and fine scattered ones around the dimples (< 5 μm). As the rolling deformation increases, the quantity of subgrain boundary increases and the < 101 > orientation is more prominent. {001} < 110 > rotation-cube textures are present in ferrite phase of samples and weak Goss texture is formed in austenite pole images.

Keywords AISI 316L austenitic stainless steel · Warm rolling · Tensile property · Fracture mechanism · Deformation texture

1 Introduction

316L austenitic stainless steels are regarded as a promising material for applications in petroleum, chemical engineering, oceanographic engineering and construction industry because of their better combinations of excellent resistance to pitting and intergranular corrosion, outstanding high-temperature mechanical property and weld performance [1, 2]. However, under several critical circumstances, some factors such as temperature, concentration and PH values would enhance environmental corrosion and inevitably make stainless steel suffer from destruction [3–5]. Common types of corrosion include intergranular corrosion, stress corrosion cracking, atmospheric corrosion and seawater corrosion. Therefore, great efforts to improve the corrosion resistance are being continuously carried out, primarily by means of alloying methods such as the additions of N, Al and other alloying elements to boost the intergranular corrosion resistance [6–8]. In order to obtain a high-performance stainless steel possessing high temperature resistance and corrosion resistance, high aluminum-content austenitic stainless steel becomes a preferred competitor. Alumina film formed on the surface, owing to the better compactness and stability compared to the conventional chromium oxide film, can improve the corrosion resistance dramatically [9–11].

With the increase in the Al content, primarily responsible for forming ferrite, high volume fraction of ferrite can be formed, leading to dual phase structure existence of ferrite and austenite in stainless steel. Meanwhile, mechanical and creep resistance properties can be decreased obviously owing to a large number of ferrites. Therefore, it is of vital importance for high aluminum-content stainless steel to design reasonable compositions. 316L austenitic stainless steel with 0.7 wt.% Al exhibits excellent performance in suppressing the degradation of corrosion resistance at 550 °C up to 12 dpa (displacement

✉ Pei-qing La
pqla@lut.cn

[1] State Key Laboratory of Advanced Processing and Recycling of Non-ferrous Metal, Lanzhou University of Technology, Lanzhou 730050, Gansu, China

[2] Key Laboratory of Nonferrous Metal Alloys and Processing, Ministry of Education, Lanzhou University of Technology, Lanzhou 730050, Gansu, China

per atom) [12, 13]. Then, austenitic stainless steels may also be characterized by rather fast kinetics of grain refinement during cold working, often accompanied by martensitic transformation, which is undesired for a certain real application [14, 15]. Simultaneously, the remarkable grain refinement should be mostly proposed during large strain deformation under high flow stresses [16–18]. Hence, the research on deformation behavior under the condition of warm rolling is emerging as a fascinating means and can meet the requirements for the development of high-performance austenitic steels. However, with regard to cold and hot working widely employed by a majority of steel processing, warm rolling is uncommon in the present thermal mechanical techniques dealing with austenitic stainless steels. The objective of the present study is to investigate the microstructure evolution and mechanical properties of 316L austenitic stainless steel with aluminum addition subjected to warm rolling at 550 °C.

2 Materials and experimental procedure

The materials examined were 316L austenitic stainless steel with 1.5 wt.% Al and obtained through smelting using medium-frequency coreless induction furnace. The chemical composition of the materials is given in Table 1. The surface oxides of alloys were polished after melting. The samples with sizes of 5 mm × 35 mm × 80 mm were taken by wire-electrode cutting. Then, the samples were hot-rolled with the rolling deformation of 40%, and the surface oxides were again put away. The warm rolling was carried out on samples with the larger rolling deformation of 30, 50 and 70% at 550 °C. The thickness of hot-rolled plate is 3 mm and changes to 2.1, 1.5 and 0.9 mm, respectively, for different deformation amounts. The reduction in per pass is 0.1 mm. Subsequently, the samples were solid solution annealed at 1050 °C for 5 min and 30 min, respectively, and then water-quenched.

The tensile test was performed at room temperature according to ASTM E8 standard using a microcomputer-controlled electronic universal material tester at a cross-head speed of 0.2 mm/s. Each test was repeated three times under the same conditions, and the results took the average values. The hardness was determined using an HBRVU-187.5-type Vicker's indentation test machine. The measure on each component of the alloy was repeated six times in different areas, and the average value was determined. The samples after solution were sanded, polished and subjected to electrolytic corrosion by 50 vol.% HNO_3 solution.

The phases were analyzed using a MeF3 optical microscope and an advance X-ray diffraction (XRD, Rigaku, D/Max-2400 type) with Cu Kα radiation. The distribution of each element was analyzed by 1600 electron probe micro-analyzer (EPMA). The surface and fracture morphologies were measured using an SEM-6700F field-emission scanning electron microscope (SEM) with a backscatter electron diffraction (EBSD) unit.

3 Results and discussion

3.1 Microstructure evolution of warm rolling

Typical microstructure images of alloys with 1.5 wt.% Al by warm rolling at 550 °C, with the rolling deformation of 30, 50 and 70% and the solid solution at 1050 °C with time of 0, 5 and 30 min, respectively, can be observed in Fig. 1. It is found that the warm-rolled specimen is composed of an ashen austenite matrix and a gray black ferrite phase. The latter exhibits the distribution pattern of strip, island and chain shapes in the matrix on which a small amount of black precipitates are also observed. Meanwhile, the microstructures are of strong orientation on the whole. The amount of big black precipitates at the phase boundary in the samples without solid solution (see Fig. 1a–c) is larger than that in the ones with solid solution treatment. Under the same condition of corrosion, compared with the samples without and with solid solution time of 30 min, it is easy for the samples with solid solution time of 5 min to present grain boundary on the matrix (see Fig. 1d–f). In another case, in contrast to the samples without and with solid solution time of 5 min, the samples with solid solution time of 30 min shows smoother and cleaner phase boundary (see Fig. 1g–i), demonstrating that long time solution is conducive to the homogeneous dissolution of carbide and growth of small crystalline grains through being swallowed by big grains. Furthermore, it can be seen that with the increasing amount of deformation, black ferrite phase is elongated and narrowed gradually.

Figure 2 shows the X-ray diffraction patterns for alloys with different solid solution time at 1050 °C. It can be

Table 1 Chemical composition of investigated steel (wt.%)

Al	C	Cr	Ni	Mo	Mn	Cu	Si	N	Fe
1.5	0.016	16.08	9.95	1.96	1.09	0.03	0.50	0.032	Balance

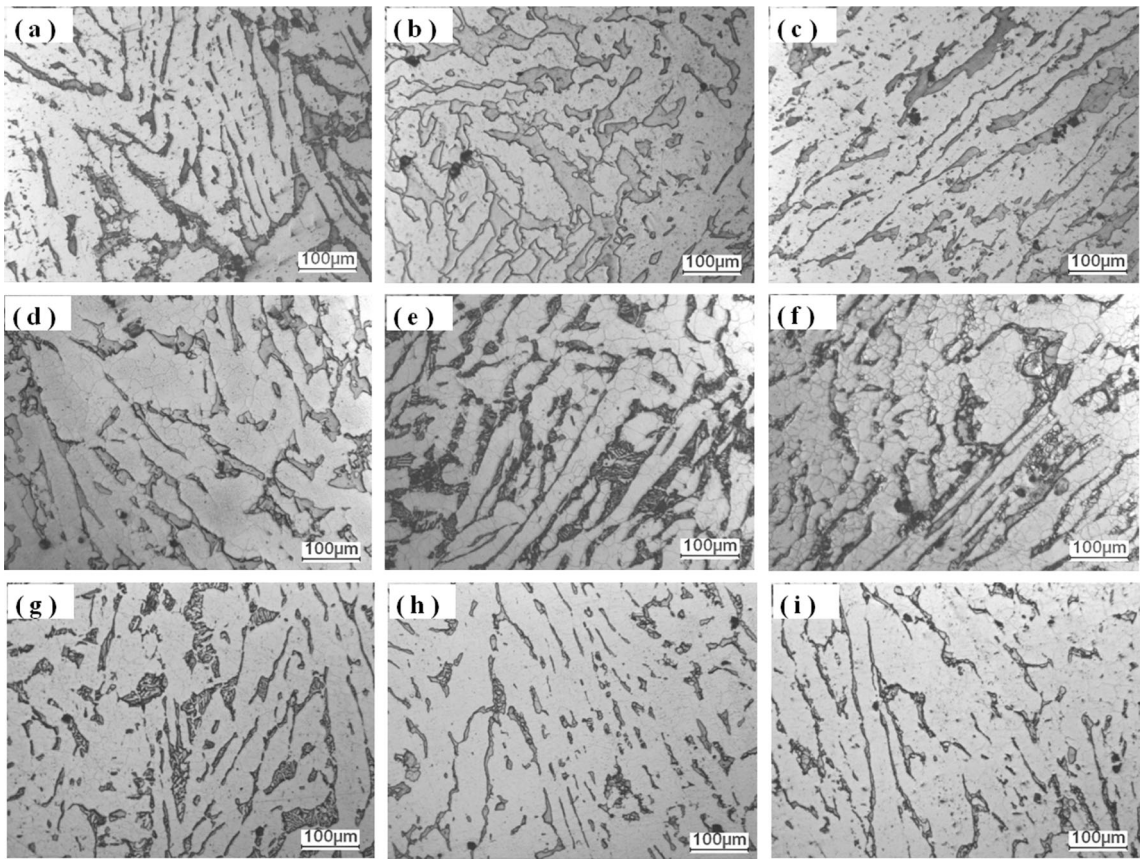

Fig. 1 Optical micrograph of samples with rolling deformation amounts of 30% (**a**, **d**, **g**), 50% (**b**, **e**, **h**) and 70% (**c**, **f**, **i**) and solution time of 0 min (**a**–**c**), 5 min (**d**–**f**) and 30 min (**g**–**i**)

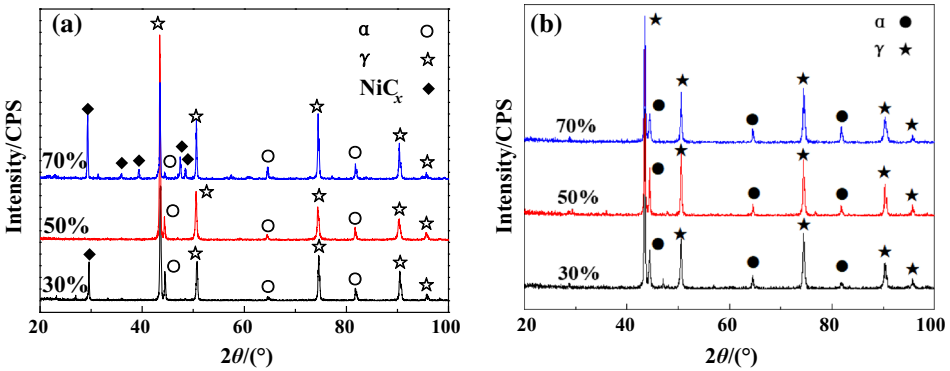

Fig. 2 X-ray diffractions of samples with solid solution time of 5 min (**a**) and 30 min (**b**)

observed that the prepared samples are mainly composed of ferrite and austenitic phases. In the case of samples subjected to solid solution treatment of 5 min, a small number of NiC_x compounds appear with deformation amounts of 30 and 70%. In order to further determine the phase composition, the electron probe microanalysis technique is employed to measure the change of element composition for the samples with the rolling deformation of 70% with respect to different solid solution time. As shown in Fig. 3, according to the distributions of Cr and Ni elements, it can be determined that white and gray phases are austenite and ferrite, respectively, in backscattered electron image. The black precipitate primarily consists of AlN and a small amount of Al_4C_3 phase because the binding strength between aluminum and carbon is much smaller than that between iron and carbon in terms of the atomic properties of aluminum [19], leading to the low solubility of carbon in aluminum element and the presence

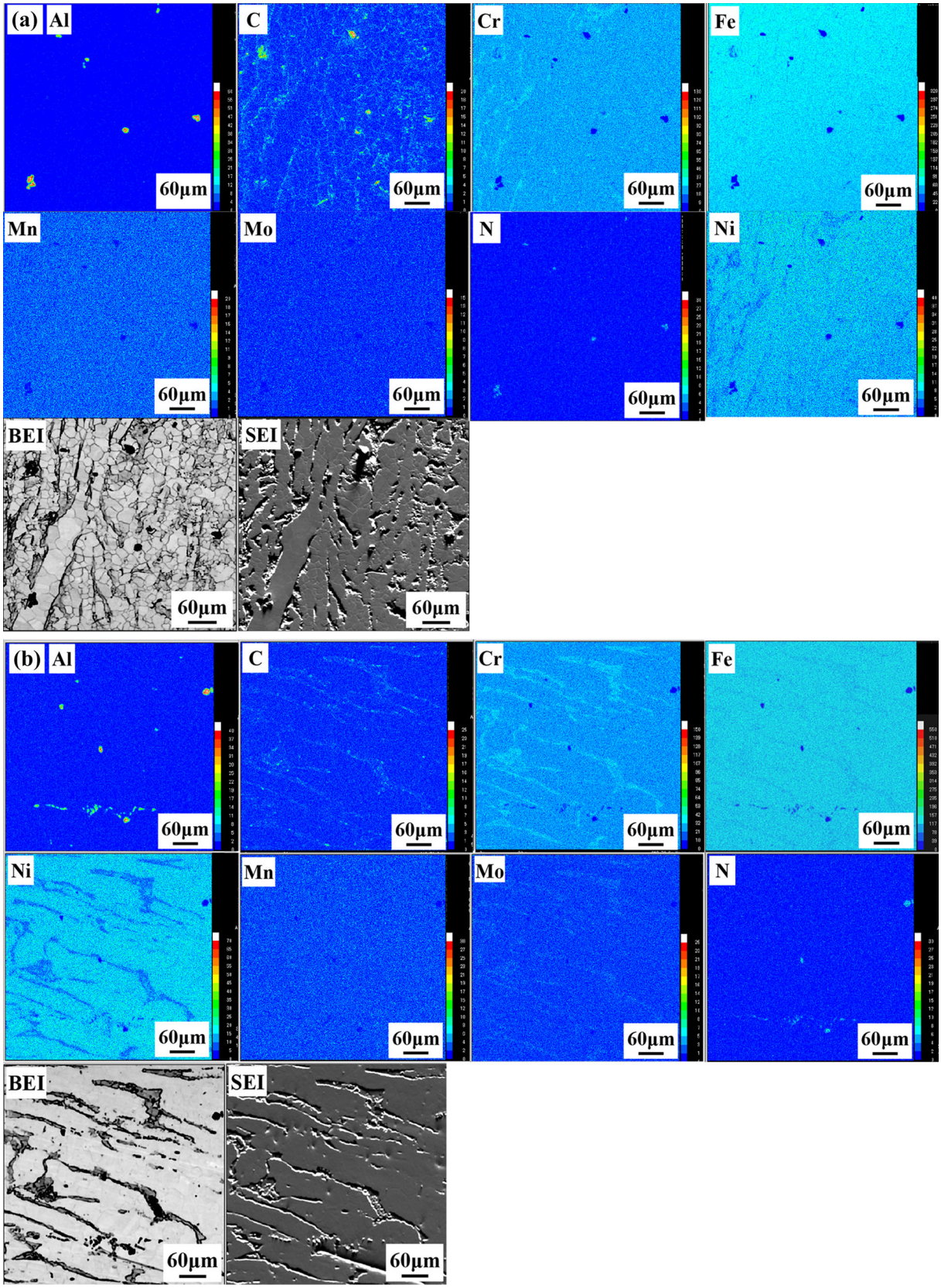

Fig. 3 EPMA and elemental distributions of warm-rolled samples with rolling deformation of 70% and solid solution time of 5 min (**a**) and 30 min (**b**)

of a bit of Al_4C_3 phase. For another reason, by means of Hume-Rothery rule [20], the fact that the difference between the atomic radiuses is below 15% is beneficial to the occurrence of solid solution behavior. AlN compounds are thus formed by the combination of Al and atmospheric N elements with the atomic radiuses of 0.143 and 0.074 nm, respectively, owing to the large radius difference of 48%. From the distribution of C element, it can be seen that obvious carbon segregation located at grain boundary was present when solid solution time is 5 min (see Fig. 3a), but it cannot be observed when solid solution time is 30 min (see Fig. 3b), and it demonstrates that some compounds such as NiC_x and $M_{27}C_3$ are probably formed, leading to the poor Cr content around grain boundaries. Thus, under the same conditions, the grain boundary (see Fig. 3a) is more likely to be exposed in the sample with solid solution time of 5 min than in other samples.

3.2 Surface microstructure of warm rolling

Figure 4 displays SEM images of surface microstructures of samples subjected to warm rolling at 550 °C with the rolling deformation of 30, 50 and 70% and the solid solution time of 0, 5 and 30 min, respectively. The samples, displaying the microstructure of grain-stretched, are composed of jet black austenite and light black ferrite. Plastic deformation occurred when samples are subjected to pressure of rolling in the course of warm rolling. Because the degree of width spread is much less than that of stretching under the condition that the thickness is far less than the width of plate, the grain is elongated and the grain size decreases gradually with the increase in rolling deformation. The number of structure defects such as dislocation density and vacancy density increases distinctly in this evolution of internal structure, and this kind of defect can be removed by solid solution. The average grain sizes are 19.97, 19.94 and 14.00 μm (calculated by the software of NanoMeasurer 1.2), for samples with the solid solution time of 5 min, and then come to 21.62, 19.66 and 19.49 μm, respectively, for samples with the solid solution time of 30 min, indicating that the effect of solid solution time on grain size is not obvious.

The statistical ferrite content of samples subjected to different rolling deformations and solid solution time is captured by the software IPWIN6.0 in Fig. 5. It is observed that under the same rolling deformation, the full diffusion

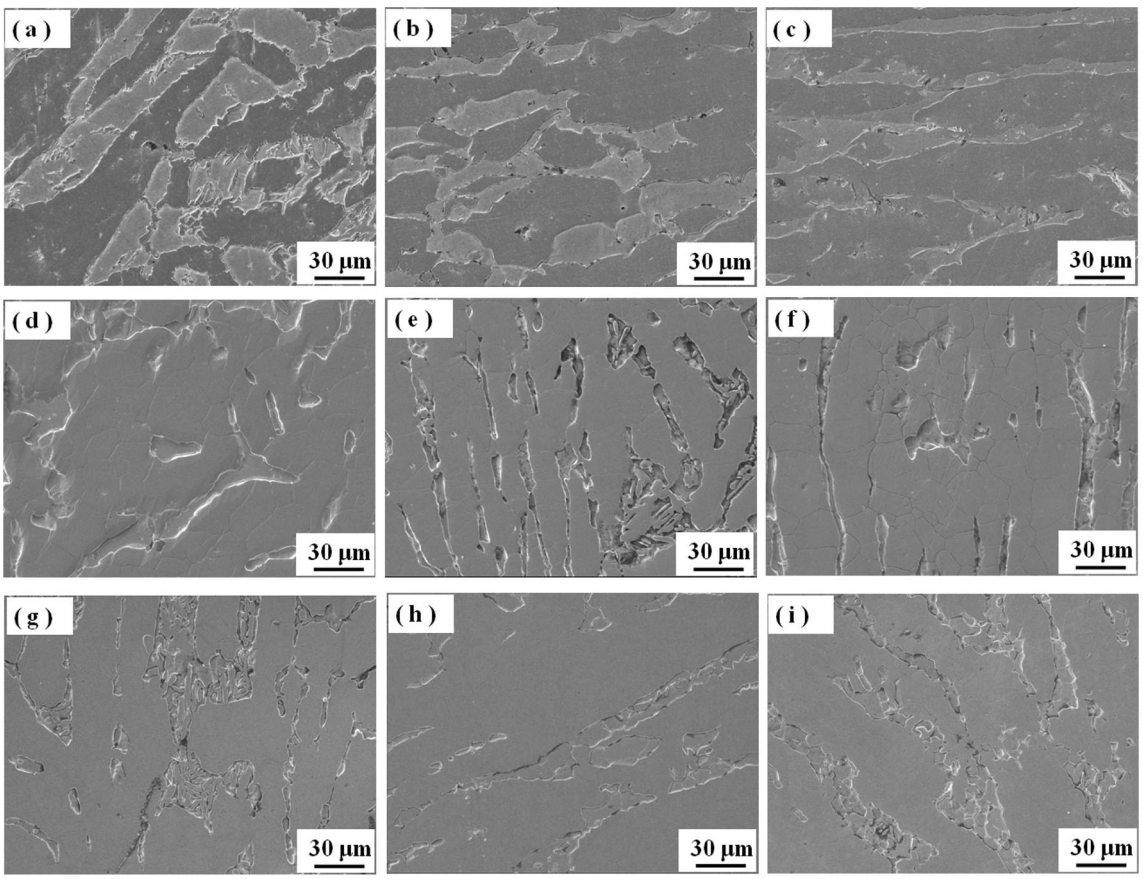

Fig. 4 Surface morphology of warm-rolled samples with deformation amounts of 30% (**a**, **d**, **g**), 50% (**b**, **e**, **h**) and 70% (**c**, **f**, **i**) and solution time of 0 min (**a**–**c**), 5 min (**d**–**f**) and 30 min (**g**–**i**) by SEM

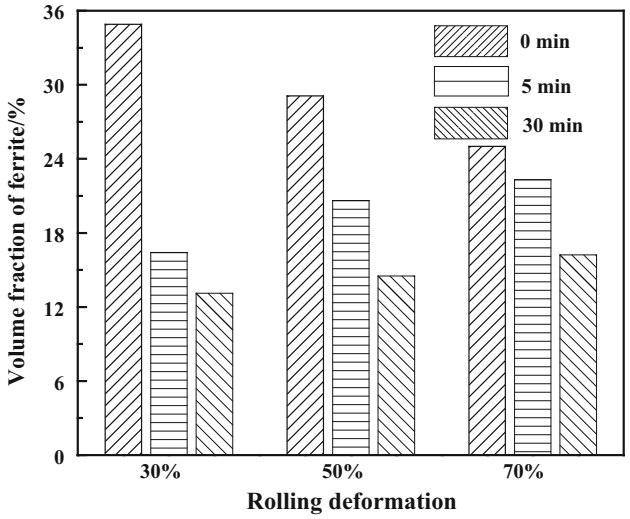

Fig. 5 Statistical ferrite content of samples subjected to different rolling deformations and solid solution times

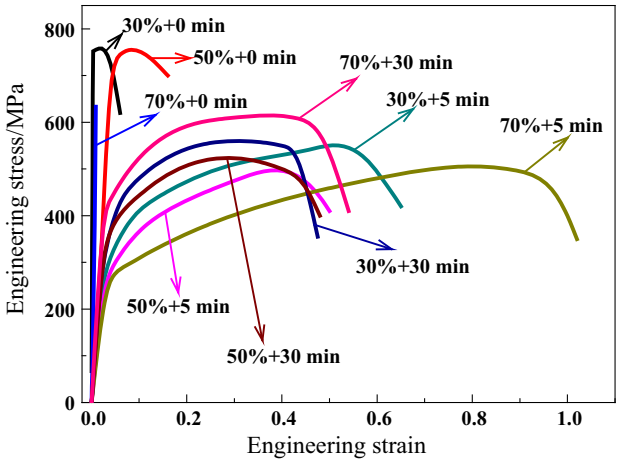

Fig. 6 Engineering stress–strain curves of 316L austenitic stainless steel with aluminum subjected to warm rolling

of Al and C atoms contributes to the austenitic transformation and the drop of ferrite content accompanying the solution time. At the identical solution time, the ferrite content also decreases, which is attributed to the rapid diffusion of alloying elements in ferrite with low atomic density and the increased number of phase interface between ferrite and austenite, leading to the diffusion distance shortening of carbon atoms in elongated ferrite transformed from chains or islands into one in samples when subjected to the condition of large deformation.

The distribution coefficients of alloying elements with different solid time and deformations are listed in Table 2. This coefficient means the ratio of element content in the ferrite to that in the austenite and is similar to that of most duplex stainless steels in the solid solution state (1040–1090 °C). The K_N (the ratio of the concentration of each element in the ferrite to that in the austenite) values of Cr, Al, Mo and N increase with increasing the solid solution time, declaring that the solubility of these alloying elements increases in the ferrite, while the K_N value of Ni has a drop showing that the solubility decreases in the austenite.

3.3 Tensile properties

Figure 6 shows the engineering stress–strain curves of high aluminum-content 316L austenitic stainless steel with different solid solution time and rolling deformations. It is found that curves consist of elastic formation, yield phase and plastic formation during the whole tensile process. The yield strength and tensile strength of samples with solid solution time of 30 min are higher than those of samples with solid solution time of 5 min when the amount of deformation is the same, while the elongation rate of the former is less than that of the latter. In the course of tension, deformation behavior in ferrite and austenite is not carried out at the same time. When the tensile stress or

Table 2 K_N values of alloying elements under different solid time and deformation amounts

Element	0 min			5 min			30 min		
	30%	50%	70%	30%	50%	70%	30%	50%	70%
Fe	0.99	1.00	0.99	0.99	0.95	1.00	0.91	0.99	0.98
Cr	1.13	1.20	1.21	1.02	1.23	1.04	1.26	1.30	1.27
Ni	0.77	0.66	0.68	0.89	0.69	0.93	0.46	0.61	0.53
Al	1.06	1.16	1.07	1.02	1.11	1.19	1.61	1.04	1.16
Mn	1.05	0.63	0.52	1.17	0.88	0.69	0.62	0.61	0.63
Mo	1.63	1.66	1.50	1.11	1.87	0.89	1.89	1.55	1.73
N	0.85	0.78	0.66	1.14	0.30	1.10	1.44	0.80	1.74

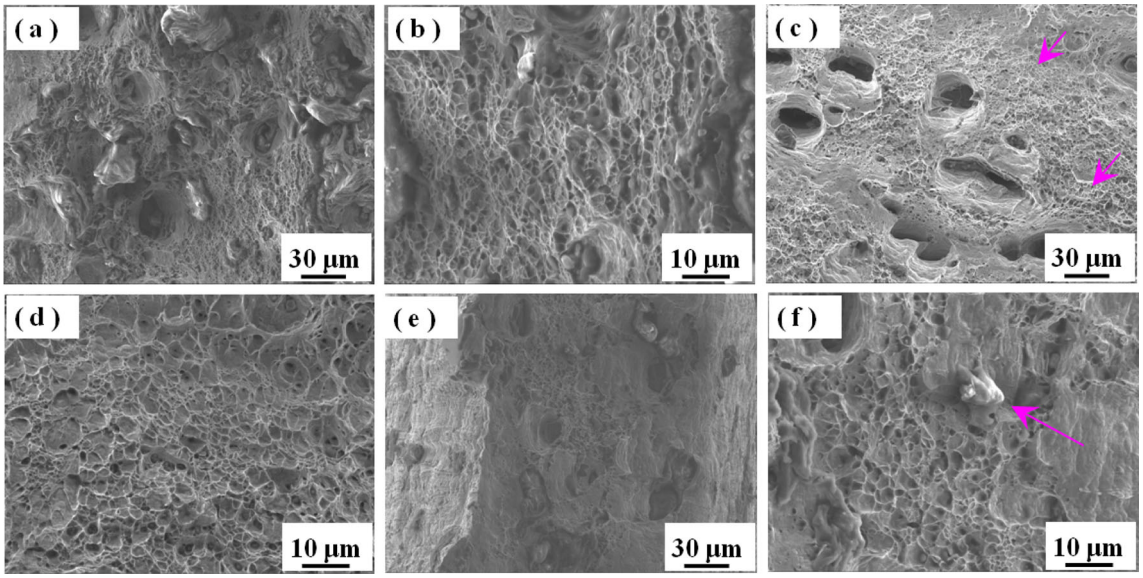

Fig. 7 Fracture micrograph of samples with solution time of 30 min and rolling deformation of 30% (**a**, **b**), 50% (**c**, **d**) and 70% (**e**, **f**)

sliding occurs in phase boundary, austenite matrix firstly yields but ferrite phase still keeps plastic deformation. The sliding or tensile stress increases gradually and would initiate cracks when the relative sliding reaches a certain degree or the tensile stress exceeds the binding force of phase boundary. Thus, the ratio of ferrite to austenite phase has a significant effect on mechanical properties. As shown in Fig. 5, the volume fraction is high without solid solution and decreases little by little with the increase in solution time, especially for lower rolling deformation. Consequently, under the same rolling deformation, the content of ferrite in samples with solution time of 30 min is lower than that in samples with solution time of 5 min. However, the former has excellent yield strength and tensile strength, which is attributed to the redistribution of precipitation and dissolution of alloying elements, as shown in Table 2. The data indicate that the K_N value of Cr increases, but that of Ni decreases, demonstrating that the concentration difference of alloying elements in ferrite and austenite phase is obvious. It can also be seen that under this condition, Cr is fully dissolved in ferrite, and Ni is fully dissolved in austenite, which means that the solid solubility of the alloying elements becomes larger. Although the content of ferrite is low in samples with solution time of 30 min, the solution-strengthening effect is distinct due to the longer solution time, making the solute atom to be fully dissolved into the matrix with little difference of average grain size. The higher lattice distortion degree caused by solution of massive solute atoms in matrix increases the resistance to dislocation motion and makes sliding difficult, improving the strength of samples with slight plasticity loss.

From the results in Fig. 6, it can be concluded that the mechanical properties of samples with solution time of 30 min are the best. In order to understand the fracture mechanism, the fracture morphology is illustrated in Fig. 7. The fracture surfaces of the samples are all composed of relatively large equal-axis ductile dimples (5–15 μm) and fine scattered ones around the dimples (> 5 μm). The fracture modes are similar and belong to toughness fracture. With regard to the large number of small dimples near the big ones in Fig. 7a, c and e, it can be deduced that more pores would be formed in the later stage of tensile process, which can delay the appearance of matrix cracks and thus produce the strong fracture resistance. The samples with rolling deformation of 30% and 70% have the higher tensile strength than the sample with rolling deformation of 50% because there are some large pits. Simultaneously, a large bulge with considerable height can be observed in Fig. 7f, as shown by an arrow, indicating that the strong pullout phenomenon is present during the tensile process, and this improves the resistance of deformation for the sample with rolling deformation of 70%, which is in agreement with the result in Fig. 6. In addition, there are some flat steps in Fig. 7c, d (indicated by arrows), demonstrating that the fracture surface consists of dimple and flat step, which leads to relatively low resistance.

3.4 Textural evolution

Some details of the evolution development of samples with solution time of 30 min and different rolling deformations are shown in Fig. 8. When the rolling deformation is 30%, the grains are uniformly deformed in the whole grain

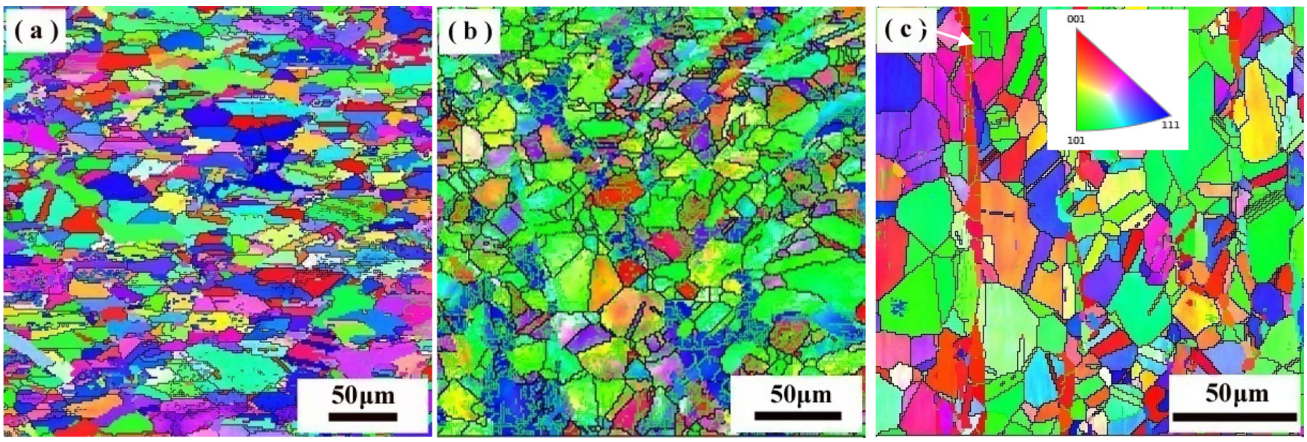

Fig. 8 EBSD orientation image maps of samples with solution time of 30 min and rolling deformation of 30% (**a**), 50% (**b**) and 70% (**c**)

boundaries; there is a certain amount of subgrain boundaries with each grain, and the crystallographic orientation is not obvious. As the rolling deformation increases to 50%, the quantity of subgrain boundary increases and the overall orientation shows distinct change, in which the $< 101 >$ orientation is more prominent. The quantity of subgrain boundary decreases, and the grain boundary is remarkable, especially for the presence of a certain amount of twinning boundary; and then, the crystallographic orientation is dominated by $< 101 >$ orientation though part of $< 001 >$ and $< 111 >$ orientations can be observed along with the rolling deformation of 70%.

Figure 9 shows the pole figures in samples with solution time of 30 min and different rolling deformations. The evolution of both austenite and ferrite deformation textures with increasing deformation was characterized by gradual crystallite rotations. It is found that $\{001\} < 110 >$ rotation-cube textures are present in ferrite phase of samples

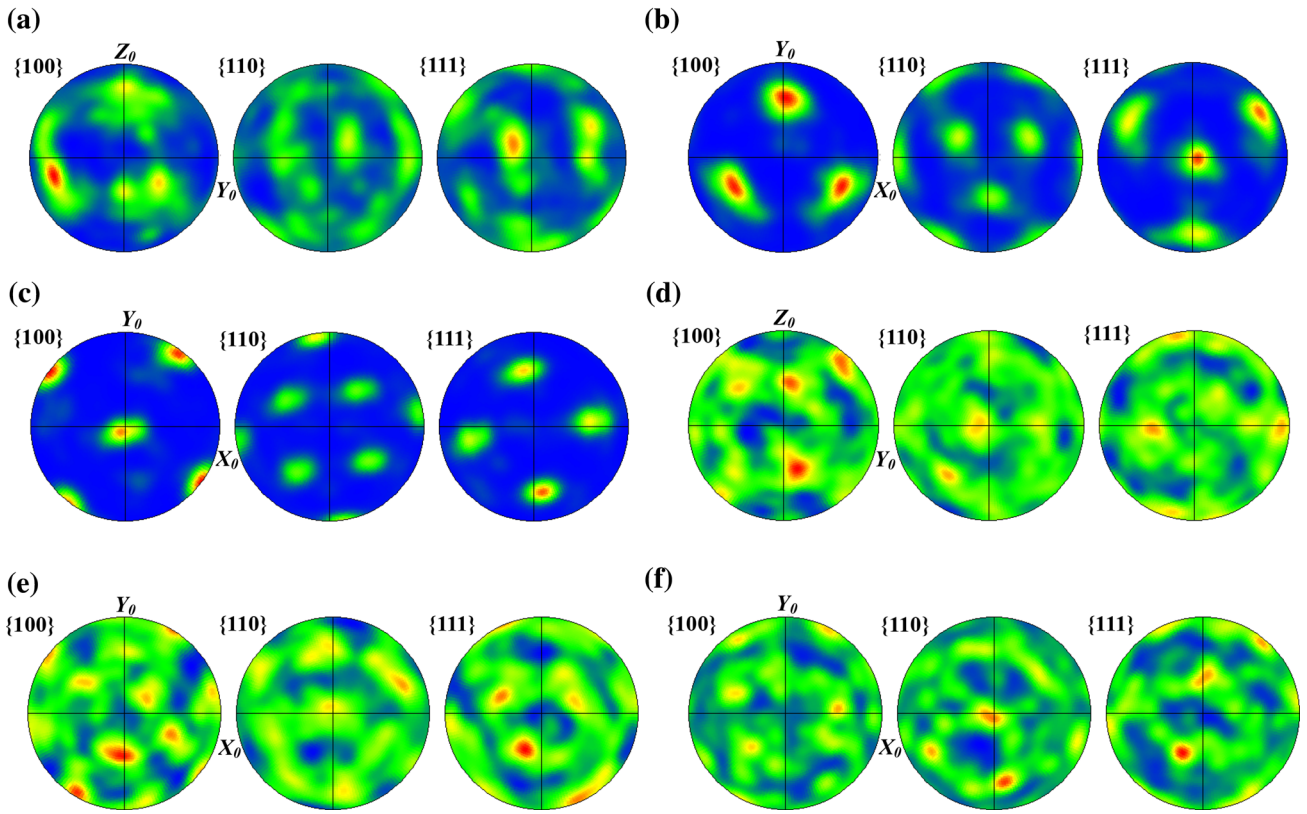

Fig. 9 Pole figures in samples with solution time of 30 min and different rolling deformations of 30% (**a**, **d**), 50% (**b**, **e**) and 70% (**c**, **f**). **a**–**c** ferrite phase; **d**–**f** austenite phase

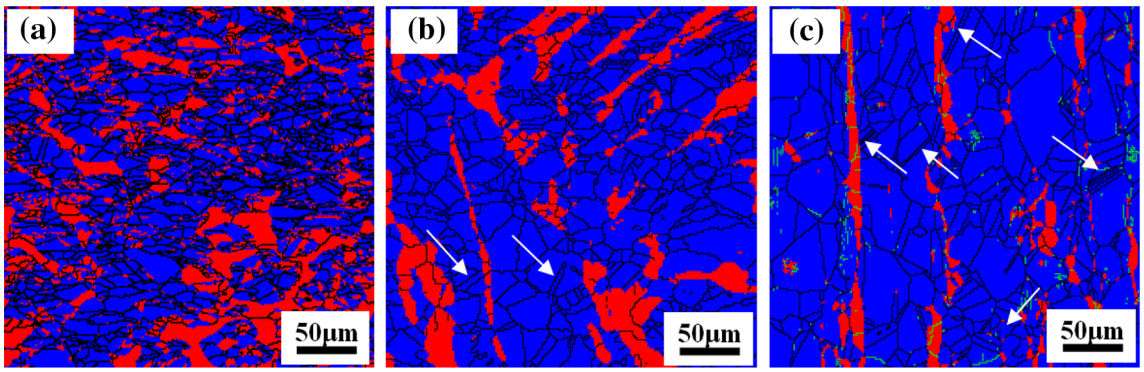

Fig. 10 Phase-contrast images of samples with rolling deformation of 30% (**a**), 50% (**b**) and 70% (**c**). *Red* ferrite; *blue* austenite

(see Fig. 9b, c) with rolling deformation of 50% and 70%, while the distinctive orientation texture cannot be observed in the sample with deformation of 30% (see Fig. 9a). This is possibly attributed to the fact that the interplanar distance of closely packed atomic plane {110} is difficult to concentrate when the subjected external force is not enough, while the other two planes are inverse. As increasing the deformation amount, the crystallite rotated gradually and formed the $\{001\} < 110 >$ rotation-cube textures finally. At the same time, for austenite pole image, there is a weak orientation texture of Goss ($\{011\} < 100 >$) in sample with increasing the rolling reduction. Texture component of Goss is frequently found in deformed and recrystallized pure fcc materials with low stacking-fault energy. Goss component is more strengthened for 70% rolling reduction compared to others, which is believed to be facilitated by the formation of twinning as shown in Fig. 8. The main twin in the fcc structure exhibits a 60° rotation around $< 111 >$ crystal axis. Considering a boundary as a coherent twin boundary, not only the rotation should be corrected, but also a boundary should be coincided with the twinning plane [21].

Phase-contrast images of samples with different rolling deformations are demonstrated in Fig. 10. It can be seen that the samples are composed of ferrite and austenite phases after warm rolling. The ferrite is distributed in the austenite matrix in the form of an island; with the increase in the deformation, the grain is refined and the volume fraction decreases; simultaneously, the island distribution gradually transforms into a discontinuous chain distribution. The grain boundary of austenite is obvious, and a few of twin boundaries (shown as white arrows) emerge with the increase in rolling deformation. There is no martensite in the course of deformation, which is also verified by data in XRD. The presence of twinning should be attributed to a certain relationship between the deformation stress and the stacking-fault energy level. The lower the stacking-fault energy, the lower is the twinning stress. Although the addition of Al would increase the stacking-fault energy to a certain extent, the stacking-fault energy can still maintain a relatively low level because the Al content is relatively low, leading to the formation of twins under action of austenite sliding. As the formation of mechanical twins involves the creation of new crystal orientation, twins gradually reduce the effective mean free path of dislocation, known as dynamic Hall–Petch effect. This effect increases the flow stress, and necking is suppressed during tensile deformation due to the highly sustained strain-hardening rate [22, 23]. Therefore, the sample with rolling deformation of 70% and solution time of 30 min can obtain high tensile strength and toughness properties.

4 Conclusions

1. The warm-rolling sample consists of an ashen austenite matrix and a gray black ferrite phase. The latter exhibits the distribution pattern of strip, island and chain shapes in the matrix, on which a small amount of black precipitates, primarily consisting of AlN and a small amount of Al_4C_3, are also observed.
2. The average grain sizes are 21.62, 19.66 and 19.49 μm for samples with the rolling deformation of 30%, 50% and 70%, respectively. The yield strength and tensile strength of samples with solid solution time of 30 min are higher than those of samples with solid solution time of 5 min when the amount of deformation is the same, while the elongation rate of the former is less than that of the latter.
3. The fracture modes are similar and belong to toughness fracture. The fracture surfaces of the samples are all composed of relatively large equal-axis ductile dimples (5–15 μm) and fine scattered ones around the dimples (< 5 μm).
4. As the rolling deformation increases to 50%, the quantity of subgrain boundary increases and the overall orientation has distinct change, in which the $< 101 >$ orientation is more prominent. $\{001\} < 110 >$

rotation-cube textures are present in ferrite phase of samples with rolling deformation of 50% and 70%, while the distinctive orientation texture cannot be observed in the sample with deformation of 30%. Weak Goss texture is formed in austenite pole images.

Acknowledgements The work was supported by the National Natural Science Foundation of China (51561020), the Gansu Provincial Science and Technology Support Program (1304GKCA027) and the China Postdoctoral Science Foundation (2015M572615, 2016T90959).

References

[1] L. Kuncicka, R. Kocich, T.C. Lowe, Prog. Mater. Sci. 88 (2017) 232–280.
[2] F.L. Xu, J.Z. Duan, C.G. Lin, B.R. Hou, J. Iron Steel Res. Int. 22 (2015) 715–720.
[3] M. Mirzaei, M.H. Paydar, Mater. Des. 121 (2017) 442–449.
[4] Z.G. Song, H. Feng, S.M. Hu, J. Iron Steel Res. Int. 24 (2017) 121–130.
[5] H.H. Mao, X. Qi, J. Cao, L.C. An, Y.T. Yang, J. Iron Steel Res. Int. 24 (2017) 561–568.
[6] F.K. Yan, G.Z. Liu, N.R. Tao, K. Lu, Acta Mater. 60 (2012) 1059–1071.
[7] S.G. Chowdhury, R. Singh, Scripta Mater. 58 (2008) 1102–1105.
[8] Q. Yu, C.F. Dong, J.X. Liang, Z.B. Liu, K. Xiao, X.G. Li, J. Iron Steel Res. Int. 24 (2017) 282–289.
[9] M. Martin, S. Weber, W. Theisen, T. Michler, J. Naumann, Int. J. Hydrogen Energ. 38 (2013) 5989–6001.
[10] T. Michler, J. Naumann, S. Weber, M. Martin, R. Pargeter, Int. J. Hydrogen Energ. 38 (2013) 9935–9941.
[11] L.H. Cao, C.J. Liu, Q. Zhao, M.F. Jiang, J. Iron Steel Res. Int. 24 (2017) 258–265.
[12] K. Kondo, Y. Miwa, N. Okubo, Y. Kaji, T. Tsukada, J. Nucl. Mater. 417 (2011) 892–895.
[13] S.G. Chowdhury, S. Das, P.K. De, Acta Mater. 53 (2005) 3951–3959.
[14] M. Odnobokova, A. Belyakov, R. Kaibyshev, Metals 5 (2015) 656–668.
[15] X.J. Shen, S. Tang, Y.J. Wu, X.L. Yang, J. Chen, Z.Y. Liu, R.D.K. Misra, G.D. Wang, Mater. Sci. Eng. A 685 (2017) 194–204.
[16] Z. Yanushkevich, A. Lugovskaya, A. Belyakov, R. Kaibyshev, Mater. Sci. Eng. A 667 (2016) 279–285.
[17] J.W. Park, J.W. Kim, Y.H. Chung, Scripta Mater. 51 (2004) 181–184.
[18] X.J. Shen, S. Tang, J. Chen, Z.Y. Liu, R.D.K. Misra, G.D. Wang, Mater. Des. 113 (2017) 137–141.
[19] M.P. Brady, Y. Yamamoto, M.L. Santella, L.R. Walker, Oxid. Met. 72 (2009) 311–333.
[20] U. Mizutani, H. Sato, M. Inukai, E.S. Zijlstra, Acta Phys. Pol. A 126 (2014) 531–534.
[21] M. Nezakat, H. Akhiani, M. Hoseini, J. Szpunar, Mater. Charact. 98 (2014) 10–17.
[22] P. Behjati, A. Kermanpur, L.P. Karjalainen, A. Jarvenpaa, M. Jaskari, H.S. Baghbadorani, A. Najafizadeh, A. Hamada, Mater. Sci. Eng. A 650 (2016) 119–128.
[23] M. Gzyl, R. Pesci, A. Rosochowski, S. Boczkal, L. Olejnik, J. Mater. Sci. 50 (2015) 2532–2543.